





Settling of inertial nonspherical particles in wavy flow

Laura K. Clark ¹, Michelle H. DiBenedetto ^{2,3}, Nicholas T. Ouellette ¹
and Jeffrey R. Koseff ¹

¹*The Bob and Norma Street Environmental Fluid Mechanics Laboratory, Department of Civil and Environmental Engineering, Stanford University, Stanford, California 94305, USA*

²*Department of Physical Oceanography, Woods Hole Oceanographic Institution, Woods Hole, Massachusetts 02543, USA*

³*Department of Mechanical Engineering, University of Washington, Seattle, Washington 98115, USA*



(Received 3 July 2020; accepted 17 November 2020; published 4 December 2020)

Microplastics are an increasingly significant problem in the world's oceans. They are transported by various ocean phenomena, one of the most fundamental of which is surface gravity waves. Since microplastics are irregularly shaped and are not typically neutrally buoyant, understanding the settling of negatively buoyant, nonspherical plastic particles under surface gravity waves is important for accurately predicting the fate of microplastics in the ocean. Here we experimentally investigate the settling of plastic rods, disks, and spheres in wavy flows. We find that the average vertical velocities of the particles can both increase and decrease in waves, relative to the particle settling velocity in quiescent flow. This variation is a function of the flow inertia at the length scale of the particle, which we characterize with a particle Reynolds number, Re_p , and is also a function of particle shape. We further examine the average vertical particle velocities by looking at two factors contributing to their behavior: The relative velocities between the particles and the flow and the manner in which the particles sample the flow. We find that the average relative velocities between the particles and the flow remain constant with Re_p , even though the variation of the relative velocities of the rods with orientation increases with increasing Re_p . The observed variation of the average vertical particle velocities with Re_p can be explained instead by how the particles sample the flow, as each of the particle shapes nonuniformly sample the flow as a function of Re_p . Accounting for the variation of particle settling velocities with shape and inertia in models is necessary to improve the accuracy of predictions of the transport of microplastics in the ocean.

DOI: [10.1103/PhysRevFluids.5.124301](https://doi.org/10.1103/PhysRevFluids.5.124301)

I. INTRODUCTION

Transport of particulate matter in the ocean, such as microorganisms [1–3], marine snow [4,5], sediment flocs [6,7], and seagrass pollen [8,9], has long been studied as these particles are not necessarily flow tracers. More recently, the discussion has come to include microplastics—millimeter-scale plastic particles with a wide variety of shapes that are scattered throughout the world's oceans [10,11]. Microplastics in the ocean are a growing problem, and understanding how they are transported by ocean flows is important to accurately assessing and mitigating their environmental impacts. Neither microplastics nor other types of particulate matter in the ocean can be characterized as being pointlike, spherical, or neutrally buoyant. Therefore, both their shape and inertia are likely relevant for determining their motion, as is well known to be true for small particles in both quiescent and turbulent flow. In quiescent flow, it has been shown that a particle's shape

and associated settling orientation affects the drag coefficient [12], potentially reducing the settling velocity by a factor of up to 1.5 [13,14]. In turbulent flows, the drag coefficient is also dependent on shape [15,16], and particles can preferentially sample the flow based on both inertia [17] and shape [18].

However, the flows in the ocean that govern the transport of particulate matter are neither quiescent nor isotropic turbulent flows. Processes affecting microplastic transport in the open ocean or coastal areas include Ekman transport, mesoscale eddies, internal tides, river plumes, and coastal fronts [19]. Near the ocean surface, gravity waves play a significant role in transport [20,21]. The motion of fluid particles in waves can be characterized according to linear wavy theory in an Eulerian framework as closed orbitals decaying with depth. These orbitals are circular in deep water and ellipsoids that flatten with depth in shallow water. Using a Lagrangian framework shows that there is a mean current associated with waves known as Stokes drift [22]. Stokes drift can significantly affect plastic transport in both the open ocean [23] and coastal areas [24].

Since approximately 40% of plastic produced has a density greater than seawater [25], and the density of originally buoyant microplastics is often increased by biofouling [26], the way that these anisotropic particles settle in wavy flows is also key to understanding their fate in the ocean. Studies that have investigated the settling velocities of microplastics have focused primarily on microplastics in quiescent fluid [27,28]. However, given that waves are known to affect the settling velocities of spherical particles (e.g., Ref. [29]), we expect that the settling of microplastics will also be influenced by wavy motions. Analytical work has shown the importance of particle inertia to the settling velocities of spheres in waves [30] and has predicted that waves enhance the settling velocities of inertial spheres [31]. Furthermore, point particles may nonuniformly sample a wavy flow in the horizontal direction, as they tend to concentrate under wave crests [32]. Waves can also cause inertialess ellipsoidal particles to adopt preferential orientations that depend on particle shape [33,34]; and, for inertial particles, there is a competition between this wave-preferred orientation and the quiescent settling-preferred orientation [35]. Therefore, one would expect that wave characteristics, particle shape, and particle inertia may all be relevant in determining the settling velocities of microplastics in wavy flows.

Here we experimentally investigate the settling of plastic rods, disks, and spheres in wavy flows. We simultaneously imaged the motion of these plastic particles and flow tracers to determine three quantities: the total velocities of the particles, the relative velocities between the particles and the flow, and the average flow velocities sampled by the particles. We find that the vertical velocities of the particles depend both on the flow inertia at the length scale of the particle, which we characterize by a particle Reynolds number Re_p , and particle shape. These effects can largely be explained by how the particles sample the flow, as particles of all shapes nonuniformly sampled the flow in shape and Re_p -dependent ways. The average relative velocities of all of the particles remained constant with Re_p , although the relative velocities of the rods showed increased dependence on orientation as Re_p increased. These results suggest that in modeling the transport of microplastics in the ocean, particle shape and inertia should not be neglected in the settling velocities of negatively buoyant particles.

We begin by describing the experimental setup in Sec. II. In Sec. III we present and discuss our results, which are summarized in Sec. IV.

II. METHODS

We used nonneutrally buoyant, millimeter-scale plastic particles of different shapes (hereafter referred to simply as “particles”) as surrogates for the typical microplastics found in the ocean. We released these particles into a wavy flow and imaged them as they moved to obtain their positions and velocities. At the same time, we also seeded the flow with small, neutrally buoyant tracer particles (hereafter referred to as “tracers”) to obtain the velocity field of the flow itself. By imaging the particles and tracers simultaneously, we were able to determine the instantaneous relative velocities and flow sampling statistics of the plastic particles.

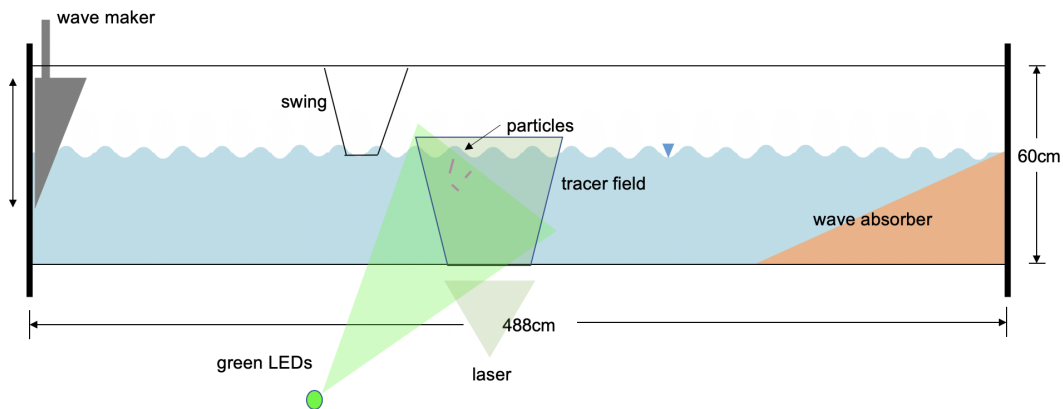


FIG. 1. Experimental setup. Waves were produced by the vertically oscillating wavemaker and dissipated by the horsehair beach. Particles were released into the flow from the swing and illuminated with green LEDs. Flow tracers were illuminated with a laser sheet.

Figure 1 shows a sketch of the experimental setup. We generated waves with a right-angled plunging wavemaker in an enclosed rectangular tank. The generated waves were laminar and fit the predictions of linear wave theory well, as demonstrated by previous studies in the same facility [35]. We considered shallow, intermediate, and deep-water waves (Table I). A horsehair beach at the far end of the tank dissipated energy and suppressed wave reflections. The dimensions of the tank were 488 cm long, 60 cm deep, and 30 cm wide, and the water was 41.5 cm deep. The flow tracers were small (45 to 53 μm diameter), neutrally buoyant, fluorescent orange polyethylene microspheres purchased from Cospheric LLC. We produced a thin laser sheet (with thickness on the order of 1 mm) coming from below the tank with an Nd:YAG laser (532 nm) to illuminate the tracers.

The particles were polystyrene spheres also purchased from Cospheric LLC and 3D-printed nylon rods and disks. The rods and disks were produced with selective laser sintering (SLS) by two 3D printing companies, Proto Labs and Sculpteo. Their properties are given in Table II. To ensure that the material properties of the particles remained constant over the course of several experiments, they were immersed in water when not in use. The rods and disks were dyed with Rhodamine 6G to make them fluorescent [36], but this was not found to be necessary for the spheres because they scattered sufficient light to make them visible. The particles were illuminated volumetrically with high-power green (530 nm) LEDs.

We placed approximately five particles of a given shape into the flow for each experimental trial. We released the rods and disks by placing them on a “swing” (a platform suspended with string near the water’s surface in the center of the tank) so that the waves carried the particles off of the swing and into the flow. Being swept off of the swing by the waves had a randomizing effect, so that the particles had no predetermined orientation or velocity. Moreover, since they tend to a shape-dependent preferred orientation [35], their initial orientations did not influence their long-term dynamics. Once the particles left the swing, it was lifted to prevent it from disturbing

TABLE I. Parameters of the different wave cases, including frequency (ω), surface amplitude (A), and wave number (k).

Wave case	ω (rad/s)	A (cm)	k (1/m)
Shallow	2π	3.5	4.3
Intermediate	3π	3.3	8.8
Deep	4π	2.3	14.1

TABLE II. Properties of particles, including density relative to that of the working fluid ($\frac{\rho_p}{\rho_f}$), aspect ratio (λ), dimensions (h and d), settling velocity in quiescent flow (w_q), and the particle settling Reynolds number defined using w_q ($\text{Re}_{p,s}$). Note that this particle Reynolds number is different than the one used in the majority of the paper and is included simply to show that the particles have comparable values of $\text{Re}_{p,s}$.

Shape	Material	$\frac{\rho_p}{\rho_f}$	λ	h (mm)	d (mm)	w_q (cm/s)	$\text{Re}_{p,s}$
Disks	Nylon 12	1.005 ± 0.001	0.16	1.15 ± 0.01	7.0 ± 0.01	0.93 ± 0.002	66
Rods	Nylon 12	1.01 ± 0.002	7.8	6.75 ± 0.04	0.86 ± 0.02	0.90 ± 0.006	60
Spheres	Polystyrene	1.02^a	1	2.96 ± 0.05	2.96 ± 0.05	2.56 ± 0.001	76

^aThe specific gravity of the spheres was 1.05, but they were placed in saltwater with a specific gravity of 1.03.

the flow. We also released some of the rods with tweezers just below the surface because they would often float on the surface when released by the swing. Because the spheres could not be deployed from the swing (they rolled off), we used a dropper to gently insert them just below the water surface.

The particles and tracers were imaged simultaneously with a Photron FASTCAM SA5 CMOS camera. The camera was fitted with a Sigma 30 mm $f/1.4$ EX DC HSM lens and an orange bandpass filter (560–600 nm). The framerate was 60 Hz, which was empirically chosen as a balance between capturing both slow and fast motion while maintaining a large field of view. The resolution of the images was 1024×1024 pixels with 18 pixels per cm. The restricted depth of field prevented particles far from the laser sheet in the transverse direction from appearing in the images. Additionally, the wavy flow is two-dimensional with little cross-stream motion according to linear wave theory. Thus, particles initially released in the plane of the laser sheet remained near it.

To process the images, we first segmented them so that we could separately determine the particle and tracer components. This was done using size as a heuristic, as the particles were significantly larger than the tracers physically, and can appear even larger in images due to fluorescence for the disks and rods and light scattering for the spheres (see Fig. 2). Rods oriented with their axis

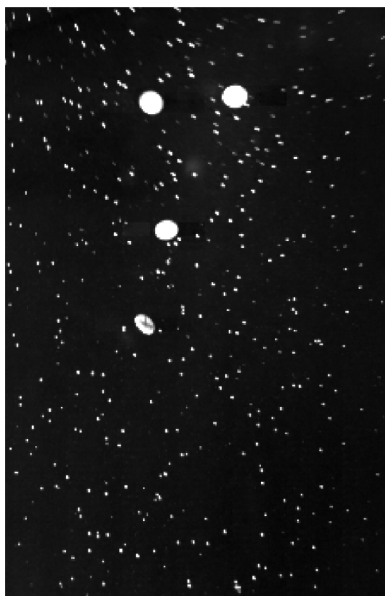


FIG. 2. Example raw image of plastic disks in the field of tracers. The disks are clearly identifiable based on their larger size, so the image can be easily separated into particle and tracer components.

of symmetry perfectly orthogonal to the plane of the waves can be mistaken for tracers with this separation technique due to their small diameters. This was not a concern for the tracer field because of the extremely low density of particles relative to tracers, but it should be noted that subsequent analysis of particle velocities is not inclusive of rods orthogonal to the plane of the waves. The background intensity fields of the separated images were then removed with an approach that accounted for lighting changes between different wave phases [35]. The velocities of the tracers and particles in the resulting images were computed by first tracking them using a predictive tracking algorithm and then convolving the trajectories with a smoothing and differentiating kernel to obtain the velocities [37]. Because the aims of this study were to isolate the effects of the waves on individual particle dynamics, we excluded the velocities of particles that were close to each other to avoid the effects of particle-particle interactions. We also excluded velocities of particles within one particle length of the tank bottom or higher than the minimum wave trough surface to avoid boundary effects. The experimental procedures described here are similar to those reported in Ref. [35], with the exception that we here imaged the particles and tracers simultaneously. This allowed us to accurately compare instantaneous quantities.

We calculated the vertical velocities of the particles relative to the local flow they experience (Δw) by interpolating the flow velocity field for a given frame (as discretely sampled by the tracers) to the locations of the centroids of the particles in that frame with cubic interpolation. Δw was then determined simply by subtracting the particle velocities (w) from the interpolated flow velocities at the particle locations.

To characterize possible effects of inertia on particle velocities, we computed the particle Reynolds number Re_p . Defining Re_p also allowed us to combine data from different wave cases. Re_p can be thought of as the Reynolds number of the flow at the length scale of the particle. We therefore defined $Re_p = (\omega a(z))l_p/\nu$, where l_p is the longest length scale of the particle, $\omega a(z)$ is a velocity scale reflective of the local vertical flow velocities produced by waves of frequency ω and amplitude $a(z)$, and ν is the kinematic viscosity of the fluid. We determined $\omega a(z)$ by fitting a sine curve to the time series of vertical velocities at a particular depth (since linear wave theory fit our experimental waves very accurately). These sine fits were computed with a vertical discretization of approximately 0.5 cm. Tracer velocities from all times and horizontal positions were included in computations of the sine fits since the wave field did not change noticeably over the time span of the experiment or over the horizontal distance illuminated by the laser sheet. Because Re_p is a local and instantaneous parameter, it was computed for each particle in each frame. Since the wave field decays with depth, Re_p typically decreases with depth as well. Note that our definition of Re_p , which uses a velocity scale of the flow to characterize the inertia of the flow at the length scale of the particle (similarly to Ref. [38], among others), is different from another common definition of the particle Reynolds number $Re_{p,s}$ that uses the relative velocity as the velocity scale (e.g., Refs. [18,39]). We list the average values of $Re_{p,s}$ based on the settling velocity of the particle in quiescent fluid in Table II to show that they are similar for the different shapes.

III. RESULTS AND DISCUSSION

We first computed the vertical velocities w of the particles in the reference frame of the tank. We normalized these velocities by the settling velocity of the particle type in quiescent fluid, so that normalized velocities $w^* > 1$ indicate particles falling faster in the presence of waves relative to still water, and $w^* < 1$ indicate particles falling more slowly in the presence of waves. The settling velocities of the particles in quiescent fluid were determined experimentally simply by taking the mean of the vertical velocities of the particles falling in the tank without waves, with only particles in the bottom half of the tank included in this mean so that the particles had time to approach their terminal velocity. We binned w^* by Re_p , thereby including the data from different wave cases and different depths, and took the mean of each bin. Figure 3 shows the resulting plot. We did not see a statistically significant difference between the wave cases when the data from each wave case was

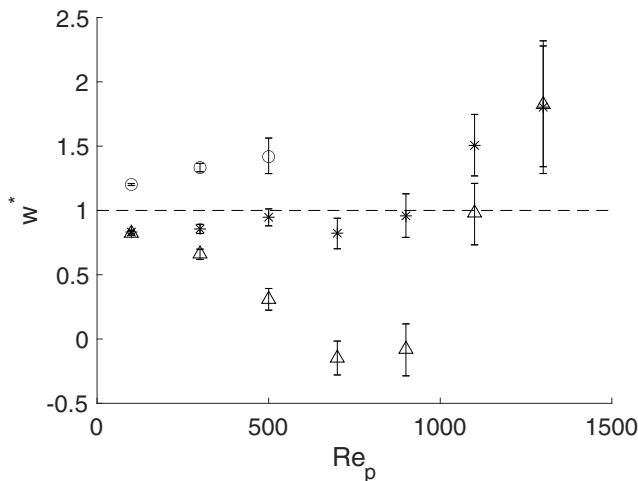


FIG. 3. Normalized particle vertical velocities w^* vs particle Reynolds number Re_p . Circles (\circ) represent spheres, asterisks ($*$) represent disks, and triangles (Δ) represent rods. Error bars show the 95% confidence intervals computed with bootstrapping. Spheres have a smaller range of Re_p values because of their smaller length scale.

plotted separately for this and subsequent plots. The error bars on this and subsequent plots show the 95% confidence intervals computed with bootstrapping [40].

For $Re_p < 200$, w^* for all of the shapes is close to one. This is to be expected: Where the flow is the weakest, the particle velocities should be close to their values in quiescent fluid. As Re_p increases, the three particle shapes behave quite differently from one another. w^* for the spheres monotonically increases with Re_p . w^* for the disks remains relatively constant at unity, until at $Re_p \approx 1000$ where it begins to increase with Re_p . This increase is dramatic enough that it doubles their vertical velocities at the highest Re_p we measured. w^* for the rods is particularly intriguing. It decreases with Re_p for low and intermediate values, meaning the rods fall more slowly as the flow strength increases. At $Re_p = 700$ and $Re_p = 900$, the mean settling velocities of the rods appear to be slightly negative. We note, however, that a settling velocity of zero is within the experimental uncertainty for these cases. For Re_p above about 1000, w^* increases with Re_p , becoming similar to its value for the disks at the highest Re_p we measured.

To investigate the observed relationship between w^* and Re_p shown in Fig. 3, we first looked at the vertical velocities of the particles relative to the local flow they experience (Δw). These relative vertical velocities are shown as a function of Re_p in Fig. 4. As in Fig. 3, the values are normalized by the settling velocities of the particles in quiescent flow, since the settling velocity and the relative vertical velocity in quiescent flow are identical. The normalized relative velocities Δw^* appear to remain constant with Re_p for all of the particle shapes. That is, regardless of how strong the flow field is, the particles fall relative to the local flow at, on average, approximately the same velocity as they would in quiescent fluid. Therefore, the variation in the vertical particle velocities w^* with Re_p seen in Fig. 3 cannot be explained by the local relative vertical velocities of the particles Δw^* .

Although the values of Δw^* do not explain the variation in w^* with shape and Re_p (Fig. 3), probing them further can give insight as to how shape and inertia may affect particle motion. Figure 5 shows Δw^* for rods and disks as a function of particle orientation, with the data separated by Re_p . Particle orientation is defined as the angle between the long axis of the particle and the propagation direction of the waves (see Fig. 6). Particles are only included in this analysis if their axis of symmetry is aligned in the plane of the waves. An analysis of the error associated with these orientation measurements in Ref. [41] shows that the average absolute error is 1 degree. Each point on the plot represents the mean value of Δw^* binned over a particular range of Re_p and orientation.

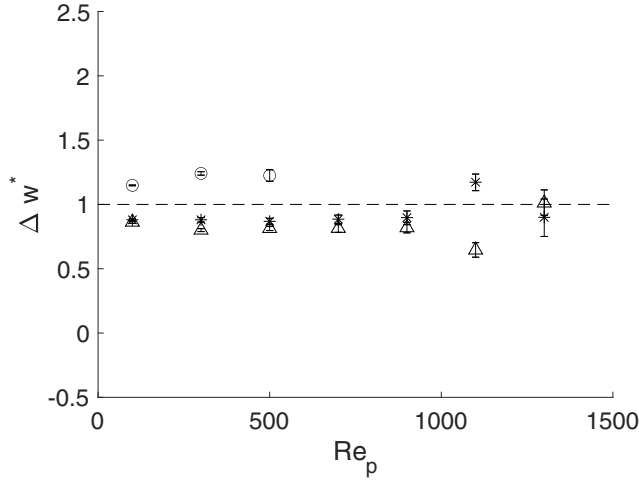


FIG. 4. Normalized relative vertical velocities Δw^* between the particles and their local flow field. As in Fig. 3, circles (\circ) represent spheres, asterisks ($*$) represent disks, and triangles (Δ) represent rods, and error bars show 95% confidence intervals.

For low Re_p , the values of Δw^* for the rods are relatively insensitive to orientation. As Re_p increases, however, the change in Δw^* for the rods with orientation also increases. The mean orientations of the rods do not change significantly with wave phase, so this variation in Δw^* at high Re_p is not due to wave phase. The orientation of a nonspherical particle controls its drag coefficient, thus affecting its relative velocity. However, the lack of a constant relationship between orientation and Δw^* across Re_p values suggests that inertia also plays an important role. The disks exhibit a smaller range of orientations than the rods, and, in further contrast to the rod case, Δw^* for the disks do not change significantly with orientation regardless of Re_p . This lack of variation in Δw^* with orientation for the disks may be because the percentage change in presented surface area of the disks due to a change in orientation is less than that of the rods, so the lift and drag on the disks can be expected to vary less with variations in orientation.

Since the behavior of the particle velocities w^* seen in Fig. 3 cannot be fully explained by the vertical relative velocities Δw^* , we investigated whether the particles preferentially sample the flow in a way that affects w^* . Preferential sampling is a well-known phenomenon in both turbulence and other types of nonuniform flows whereby particles oversample some portions of the flow field with particular qualities relative to how fluid elements would. For example, spheres that are heavier than the fluid tend to concentrate in strain-dominated regions in turbulence or cellular flow fields, while light spheres and bubbles collect in regions of intense vorticity [17,42]. Particles can also preferentially sample flow based on their shape: inertial fibers in wall-bounded turbulent flows tend to segregate into streaks correlated with lower fluid velocities [18], and the degree to which they oversample these low-velocity streaks changes with particle aspect ratio [43]. Preferential sampling can impact particle settling velocities. “Fast-tracking,” where particles preferentially sample downwashes in turbulent or vortical flows, can enhance particle settling velocities (see Refs. [44,45], among others), while nonlinear drag effects can lead to a bias toward upward velocities and effectively reduced particle settling velocities [39,46].

To determine whether our particles do in fact preferentially sample the flow field, we first considered the fraction of time the particles spend in parts of the wave with downward flow velocities. This is shown in Fig. 7(a), where the percentage of time particles spend in wave phases between 0 and π (corresponding to downward flow velocities) is plotted as a function of Re_p . A true tracer spends 50% of the time in this range of wave phases and experiences no net vertical velocity

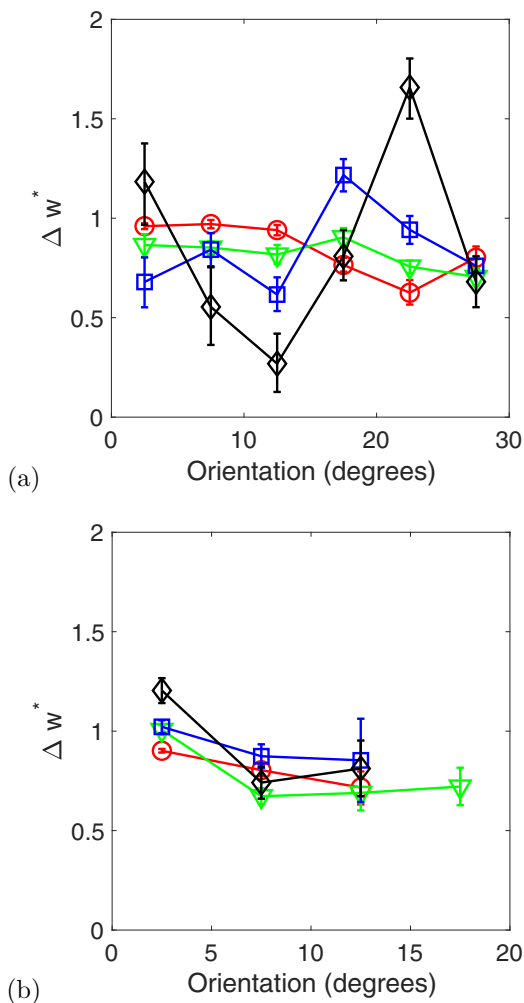


FIG. 5. Normalized relative vertical velocities Δw^* of (a) rods and (b) disks plotted against particle orientations in the plane of the waves. The different colors represent different ranges of Re_p : $0 \leq Re_p \leq 300$ (red circles \circ), $300 \leq Re_p \leq 600$ (green triangles ∇), $600 \leq Re_p \leq 900$ (blue squares \square), and $900 \leq Re_p \leq 1200$ (black diamonds \diamond). As in other figures, error bars represent the 95% confidence intervals computed by bootstrapping.

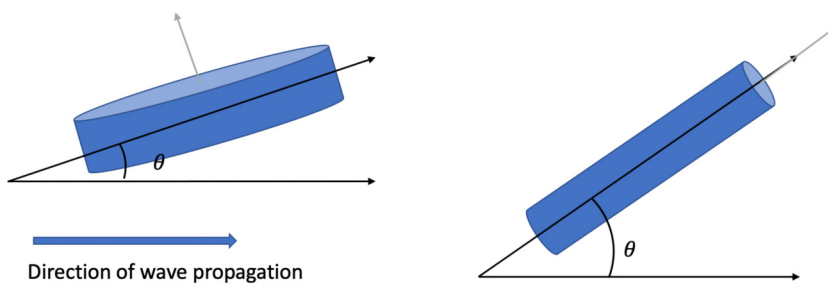


FIG. 6. Definition of orientation θ of a disk (left) and a rod (right). Axes are in the plane of the waves. Gray vectors show the axes of symmetry of the particles.

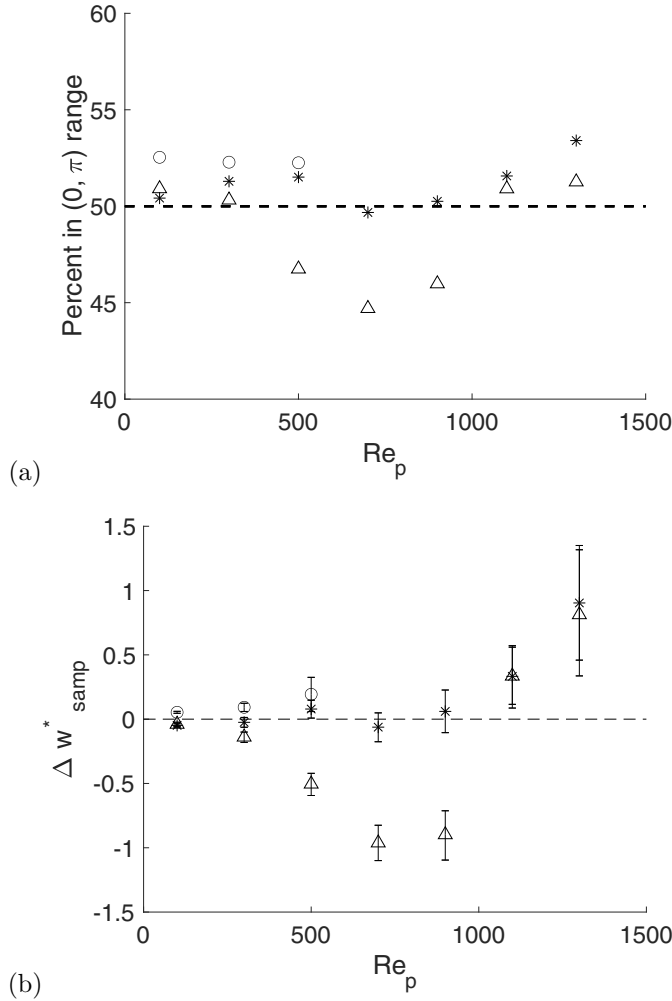


FIG. 7. (a) Percentage of time the particles spend in wave phases corresponding to downward flow as a function of Re_p . (b) Normalized preferentially sampled flow velocities Δw_{samp}^* , also as a function of Re_p , with 95% confidence intervals. In both panels, circles (\circ) represent spheres, asterisks ($*$) represent disks, and triangles (\triangle) represent rods.

according to linear wave theory, which, as previously mentioned, describes our waves well. Many of the values in the plot, especially those corresponding to the disks at high Re_p and to the rods, are not equal to 50%, so that suggests the particles are nonuniformly sampling the flow at those locations.

In order to further quantify preferential sampling, we looked more specifically at the flow velocities sampled by a particle; that is, the values of the fluid velocity field interpolated to the particle positions. Figure 7(b) shows the normalized difference between the means of the particle-sampled and tracer-sampled flow velocities, Δw_{samp}^* , as a function of Re_p :

$$\Delta w_{\text{samp}}^* = \frac{1}{w_q} \left[\frac{1}{N_p} \sum_{i=1}^{N_p} w_{f,p}^{(i)} - \frac{1}{N_t} \sum_{i=1}^{N_t} w_{f,t}^{(i)} \right],$$

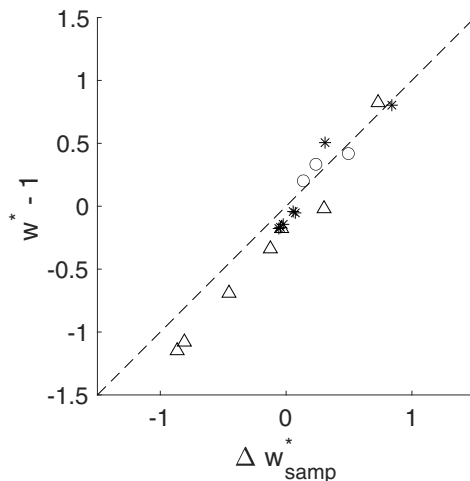


FIG. 8. Normalized settling velocities w^* minus the normalized quiescent settling velocity (1), plotted against preferentially sampled flow velocities Δw_{samp}^* . As in other figures, circles (\circ) represent spheres, asterisks ($*$) represent disks, and triangles (\triangle) represent rods.

where N_p is the number of particle velocities for a given range of Re_p , N_t is the number of virtual tracer velocities for the same range of Re_p , and $w_f^{(i)}$ represents the instantaneous flow velocities sampled by the particles [$w_{f,p}^{(i)}$] and fluid elements [$w_{f,t}^{(i)}$]. We confirmed that in these experiments fluid elements experienced no net vertical velocity by numerically tracking virtual tracers through the measured flow fields by integrating their equation of motion in time [47]. These virtual tracers were initially placed at random locations in the flow field to ensure even sampling. As expected from linear wave theory, the average vertical flow velocities experienced by the virtual tracers were approximately zero, so we set the second term in our sampling equation to zero. For consistency with Figs. 3 and 4, the values are again normalized by the quiescent settling velocities w_q of the particles. Positive values of Δw_{samp}^* indicate that particles oversample downward flow relative to the virtual tracers.

From Fig. 7, we see that the particles indeed preferentially sample the flow based on shape and Re_p . This effect is the most obvious for the rods, which oversample regions of the flow field with upward flow velocities for $Re_p < 1000$, but preferentially sample regions of downward flow at higher Re_p . The spheres slightly oversample regions of downward flow velocities, while the disks do not preferentially sample until Re_p is above 1000, at which point they begin oversampling regions of downward flow.

Combined with the near-constant relative velocities Δw^* shown in Fig. 4, the preferentially sampled flow velocities Δw_{samp}^* shown in Fig. 7(b) explain much of the behavior of the particle velocities w^* shown in Fig. 3. This can be seen clearly in Fig. 8, which shows $w^* - 1$ plotted against Δw_{samp}^* , where 1 is subtracted from w^* because it is the normalized quiescent settling velocity. Each point corresponds to a particular range of Re_p , but the specific values have not been included for readability. Different symbols indicate different particle shapes, as before. If a point is at the origin, then the particle is falling with the same w^* it would have in quiescent flow and is not sampling the flow differently from how a passive tracer would. Points along the one-to-one line indicate w^* differing from quiescent velocities proportionally to the variations in Δw_{samp}^* . From how close the data generally are to the one-to-one line, we can observe that much of the variation in w^* is indeed due to variations in how the particles sample the flow.

IV. CONCLUSION

Our experimental results show that the settling velocities of particles in wavy flows are dependent on both the flow inertia at the length scale of the particle, which we characterize with Re_p , and particle shape. The particle vertical velocities w^* can be thought of as resulting from two measurable phenomena: the vertical velocities of the particles relative to the local flow Δw^* , and the difference in the flow velocities sampled by a particle versus those sampled by a passive tracer Δw_{samp}^* . On average, Δw^* remains constant with Re_p , although the Δw^* for the rods increasingly depend on orientation as Re_p increases. Thus, the rods' shape becomes increasingly important as the flow inertia at the length scale of the rods increases. This is not the case for disks, however, perhaps because the sensitivity of presented surface area to orientation is less for disks than for rods. Unlike Δw^* , Δw_{samp}^* varies with Re_p in a different way for each shape. The combined effects of constant Δw^* and varying Δw_{samp}^* cause (i) spheres to fall more quickly with increasing Re_p ; (ii) disks to fall with the same average vertical velocity they would have in quiescent fluid up to a certain Re_p , but more quickly beyond that; and (iii) rods to fall more slowly than they would in quiescent fluid for low Re_p , but more quickly for high Re_p . These results have implications for the modeling of microplastic transport in the ocean. Microplastics are often modeled as noninertial point particles that are carried as passive tracers by ocean flows, sometimes with an additional settling velocity that may be a simple function of particle size or relative density (e.g. Refs. [48,49] and references in Ref. [19]). However, even though microplastics are small, these results show that their shape and inertia can lead to significant variation in their settling velocities. Accounting for the variation of particle settling velocities with shape and inertia in models is thus necessary to improve the accuracy of predictions of the transport of microplastics in the ocean.

ACKNOWLEDGMENTS

The authors acknowledge Alexandra Warner for help with initial experimental design and Bill Sabala and Yukinobu Tanimoto for help with experimental setup. This work was supported by the U.S. National Science Foundation under Grant No. CBET-1706586.

-
- [1] E. Lauga and T. R. Powers, The hydrodynamics of swimming microorganisms, *Rep. Prog. Phys.* **72**, 096601 (2009).
 - [2] J. S. Guasto, R. Rusconi, and R. Stocker, Fluid mechanics of planktonic microorganisms, *Annu. Rev. Fluid Mech.* **44**, 373 (2012).
 - [3] N. Pujara, M. A. R. Koehl, and E. A. Variano, Rotations and accumulation of ellipsoidal microswimmers in isotropic turbulence, *J. Fluid Mech.* **838**, 356 (2018).
 - [4] J. Ruiz, What generates daily cycles of marine snow?, *Deep Sea Res. Part I* **44**, 1105 (1997).
 - [5] T. Asaeda and E. Wolanski, Settling of muddy marine snow, *Wetlands Ecol. Manage.* **10**, 283 (2002).
 - [6] K. Black, T. Tolhurst, D. Paterson, and S. Hagerthey, Working with natural cohesive sediments, *J. Hydraul. Eng.* **128**, 2 (2002).
 - [7] L. C. van Rijn, Unified view of sediment transport by currents and waves. II: Suspended transport, *J. Hydraul. Eng.* **133**, 668 (2007).
 - [8] J. D. Ackerman, Submarine pollination in the marine angiosperm *Zostera marina* (Zosteraceae). II. Pollen transport in flow fields and capture by stigmas, *Am. J. Bot.* **84**, 1110 (1997).
 - [9] E. Follett, C. Hays, and H. Nepf, Canopy-mediated hydrodynamics contributes to greater allelic richness in seeds produced higher in meadows of the coastal eelgrass *Zostera marina*, *Front. Mar. Sci.* **6**, 8 (2019).
 - [10] I. Chubarenko, A. Bagaev, M. Zobkov, and E. Esiukova, On some physical and dynamical properties of microplastic particles in marine environment, *Mar. Pollut. Bull.* **108**, 105 (2016).
 - [11] K. L. Law, Plastics in the marine environment, *Annu. Rev. Mar. Sci.* **9**, 205 (2017).

- [12] X. Song, Z. Xu, G. Li, Z. Pang, and Z. Zhu, A new model for predicting drag coefficient and settling velocity of spherical and non-spherical particle in Newtonian fluid, *Powder Technol.* **321**, 242 (2017).
- [13] W. E. Dietrich, Settling velocity of natural particles, *Water Resour. Res.* **18**, 1615 (1982).
- [14] A. Hazzab, A. Terfous, and A. Ghenaim, Measurement and modeling of the settling velocity of isometric particles, *Powder Technol.* **184**, 105 (2008).
- [15] M. Zastawny, G. Mallouppas, F. Zhao, and B. Van Wachem, Derivation of drag and lift force and torque coefficients for non-spherical particles in flows, *Int. J. Multiphase Flow* **39**, 227 (2012).
- [16] M. N. Ardekani, G. Sardina, L. Brandt, L. Karp-Boss, R. N. Bearon, and E. A. Variano, Sedimentation of inertia-less prolate spheroids in homogenous isotropic turbulence with application to non-motile phytoplankton, *J. Fluid Mech.* **831**, 655 (2017).
- [17] S. Balachandar and J. K. Eaton, Turbulent dispersed multiphase flow, *Annu. Rev. Fluid Mech.* **42**, 111 (2010).
- [18] G. A. Voth and A. Soldati, Anisotropic particles in turbulence, *Annu. Rev. Fluid Mech.* **49**, 249 (2017).
- [19] E. Van Sebille, S. Aliani, K. L. Law, N. Maximenko, J. M. Alsina, A. Bagaev, M. Bergmann, B. Chapron, I. Chubarenko, A. Cózar *et al.*, The physical oceanography of the transport of floating marine debris, *Environ. Res. Lett.* **15**, 023003 (2020).
- [20] J. Röhrs, K. H. Christensen, F. Vikebø, S. Sundby, Ø. Saetra, and G. Broström, Wave-induced transport and vertical mixing of pelagic eggs and larvae, *Limnol. Oceanogr.* **59**, 1213 (2014).
- [21] M. Drivdal, G. Broström, and K. H. Christensen, Wave-induced mixing and transport of buoyant particles: Application to the Staffjord a oil spill, *Ocean Sci.* **10**, 977 (2014).
- [22] G. G. Stokes, On the theory of oscillatory waves, *Trans. Cambridge Philos. Soc.* **8**, 441 (1880).
- [23] V. Onink, D. Wichmann, P. Delandmeter, and E. Van Sebille, The role of Ekman currents, geostrophy, and stokes drift in the accumulation of floating microplastic, *J. Geophys. Res.: Oceans* **124**, 1474 (2019).
- [24] A. Isobe, K. Kubo, Y. Tamura, E. Nakashima, N. Fujii *et al.*, Selective transport of microplastics and mesoplastics by drifting in coastal waters, *Mar. Pollut. Bull.* **89**, 324 (2014).
- [25] R. Geyer, J. R. Jambeck, and K. L. Law, Production, use, and fate of all plastics ever made, *Sci. Adv.* **3**, e1700782 (2017).
- [26] A. L. Andrady, Microplastics in the marine environment, *Mar. Pollut. Bull.* **62**, 1596 (2011).
- [27] L. Khatmullina and I. Isachenko, Settling velocity of microplastic particles of regular shapes, *Mar. Pollut. Bull.* **114**, 871 (2017).
- [28] K. Waldschläger and H. Schüttrumpf, Effects of particle properties on the settling and rise velocities of microplastics in freshwater under laboratory conditions, *Environ. Sci. Technol.* **53**, 1958 (2019).
- [29] M. Bakhoday-Paskyabi, Particle motions beneath irrotational water waves, *Ocean Dyn.* **65**, 1063 (2015).
- [30] I. Eames, Settling of particles beneath water waves, *J. Phys. Oceanogr.* **38**, 2846 (2008).
- [31] F. Santamaria, G. Boffetta, M. M. Afonso, A. Mazzino, M. Onorato, and D. Pugliese, Stokes drift for inertial particles transported by water waves, *Europhys. Lett.* **102**, 14003 (2013).
- [32] M. H. DiBenedetto, Non-breaking wave effects on buoyant particle distributions, *Front. Mar. Sci.* **7**, 148 (2020).
- [33] M. H. DiBenedetto, N. T. Ouellette, and J. R. Koseff, Transport of anisotropic particles under waves, *J. Fluid Mech.* **837**, 320 (2018).
- [34] M. H. DiBenedetto and N. T. Ouellette, Preferential orientation of spheroidal particles in wavy flow, *J. Fluid Mech.* **856**, 850 (2018).
- [35] M. H. DiBenedetto, J. R. Koseff, and N. T. Ouellette, Orientation dynamics of nonspherical particles under surface gravity waves, *Phys. Rev. Fluids* **4**, 034301 (2019).
- [36] B. C. Cole, G. G. Marcus, S. Parsa, S. Kramel, R. Ni, and G. A. Voth, Methods for measuring the orientation and rotation rate of 3D-printed particles in turbulence, *J. Vis. Exp.* (2016) e53599.
- [37] D. H. Kelley and N. T. Ouellette, Using particle tracking to measure flow instabilities in an undergraduate laboratory experiment, *Am. J. Phys.* **79**, 267 (2011).
- [38] H. Xu and E. Bodenschatz, Motion of inertial particles with size larger than kolmogorov scale in turbulent flows, *Physica D* **237**, 2095 (2008).
- [39] G. Good, P. Ireland, G. Bewley, E. Bodenschatz, L. Collins, and Z. Warhaft, Settling regimes of inertial particles in isotropic turbulence, *J. Fluid Mech.* **759**, R3 (2014).

- [40] B. Efron and R. Tibshirani, Bootstrap methods for standard errors, confidence intervals, and other measures of statistical accuracy, *Stat. Sci.* **1**, 54 (1986).
- [41] M. H. DiBenedetto, Transport and Behavior of Non-spherical Particles in Waves, Ph.D. thesis, Stanford University (2019).
- [42] M. R. Maxey, The gravitational settling of aerosol particles in homogeneous turbulence and random flow fields, *J. Fluid Mech.* **174**, 441 (1987).
- [43] F. Zhao, W. K. George, and B. G. M. Van Wachem, Four-way coupled simulations of small particles in turbulent channel flow: The effects of particle shape and Stokes number, *Phys. Fluids* **27**, 083301 (2015).
- [44] M. R. Maxey and S. Corrsin, Gravitational settling of aerosol particles in randomly oriented cellular flow fields, *J. Atmos. Sci.* **43**, 1112 (1986).
- [45] C. Yang and U. Lei, The role of the turbulent scales in the settling velocity of heavy particles in homogeneous isotropic turbulence, *J. Fluid Mech.* **371**, 179 (1998).
- [46] L.-P. Wang and M. R. Maxey, Settling velocity and concentration distribution of heavy particles in homogeneous isotropic turbulence, *J. Fluid Mech.* **256**, 27 (1993).
- [47] N. T. Ouellette, P. J. J. O'Malley, and J. P. Gollub, Transport of Finite-Sized Particles in Chaotic Flow, *Phys. Rev. Lett.* **101**, 174504 (2008).
- [48] A. S. Mountford and M. A. Morales Maqueda, Eulerian modeling of the three-dimensional distribution of seven popular microplastic types in the global ocean, *J. Geophys. Res.: Oceans* **124**, 8558 (2019).
- [49] L.-M. Lebreton, S. Greer, and J. Borrero, Numerical modeling of floating debris in the world's oceans, *Mar. Pollut. Bull.* **64**, 653 (2012).